The importance of molecular structure and functionalization of oxo-graphene sheets for gene silencing

Giacomo Reina [a,1], Cristian Gabellini [b], Maria Maranska [c], Fabian Grote [c], Shan Min Chin [d],
Lucas Jacquemin [a], François Berger [d], Paola Posocco [b], Siegfried Eigler [c], Alberto Bianco [a,*]

[a] CNRS, Immunology, Immunopathology and Therapeutic Chemistry, UPR3572, University of Strasbourg, ISIS, 67000, Strasbourg, France
[b] Department of Engineering and Architecture, University of Trieste, 34127, Trieste, Italy
[c] Institute of Chemistry and Biochemistry, Freie Universität Berlin, Takustraße 3, 14195, Berlin, Germany
[d] INSERM UMR1205, Brain Tech Lab, Grenoble Alpes University, Grenoble, 38000, France

ARTICLE INFO

ABSTRACT

Gene therapy has recently reached the front line in the treatments of different diseases. Although graphene oxide has been widely used as a gene vector, its clinical application is limited by the scarce inhomogeneity of the different synthetic methods. Recently, we have developed the preparation of a new class of graphene oxide, named oxo-G, obtained by a rigorous synthetic method with controlled size and surface chemistry. oxo-G has been successfully applied for the production of reduced graphene oxide with remarkable conductivity. Here, we applied oxo-G to gene delivery. After *ad hoc* functionalization, we found that oxo-G is able to efficiently complex siRNA and strongly induce gene silencing *in vitro* at five pg/cell doses, more than 20 times lower than the best results reported in the literature using graphene-based materials. The aim of this work is to inspire the readers to develop further oxo-G materials for biomedical applications. We hope that oxo-G can be considered as an alternative candidate in future gene silencing use *in vivo*.

1. Introduction

Gene therapy is becoming an alternative therapeutic modality for the treatments of different pathologies [1]. This sophisticated technology inspired by viruses foresees the delivery of the genetic material (typically a DNA or a RNA fragment) that punctually re-programs cell activity up or down, regulating an endogenous selected gene, or inserting exogenous genes for the production of new desired proteins [1]. At the moment, different gene delivery-based strategies have been approved by FDA treating diseases associated to immune system dysfunctions. For instance, chimeric antigen receptor (CAR)-T cell immunotherapy was approved in 2020 to treat different blood cancers [2]. For this therapy, T-cells acquired from a donor are "trained" through gene therapy to express the selected CAR that efficiently targets cancer cells [2]. More recently, the first generation gene therapy vaccines have been reported for the treatment SARS-CoV-2 pandemic [3]. Gene therapy has also been explored for the treatment of other diseases, including several kinds of cancers [4]. The main soft spot for gene therapy wider application relies on the gene vector. Indeed, exogenous nucleic acids can hardly overcome the biological barriers alone and are easily degraded once internalized into lysosomes. Many studies have been carried out on soft nanocarriers like liposomes, self-assembled amphiphilic dendrons or dendrimers. However, these synthetic vesicles may suffer from low targeting efficacy and thermal instability [1].

Hard nanomaterials (e.g., inorganic nanoparticles and carbon nanomaterials) have also been used as a shuttle in gene therapy with interesting results. In this context, graphene oxide (GO) the oxidized form of graphene, has been extensively studied for gene therapy *in vitro* and *in vivo* [5–8]. Compared to other hard and soft nanomaterials, GO displays different benefits in gene delivery. It shows high biocompatibility and can easily penetrate cell membranes [9]. Moreover, GO has a rich surface chemistry allowing it to anchor different desired molecules (e.g., drugs, targeting agents, and imaging probes) onto its surface through orthogonal multi-functionalization [10]. In addition, it has a strong photothermal

* Corresponding author.
  E-mail address: a.bianco@ibmc-cnrs.unistra.fr (A. Bianco).
[1] Present address: Graduate School of Human and Environmental Studies, Kyoto University, Sakyo-ku, Kyoto 606-8501, Japan

activity [11] when irradiated in the far-red region and can be easily biodegraded into the body [12]. Despite these indisputable advantages, there are still some concerns on the use of GO for clinical applications [13]. In particular, the chemical structure of GO is still not defined, and it strongly depends on the preparation methods [14]. GO is produced through harsh graphite oxidation that generates highly defective layers [14]. The "rush to gold" for GO production has jeopardized the preparation approaches causing a deep inhomogeneity of the final material. Recently, milder oxidation conditions have been optimized to synthesize another class of graphene oxide, namely oxo-G, with a regular chemical structure with extended graphitic domains [15]. Compared to GO, oxo-G can be considered as a defect-free carbon sheet with an almost intact σ-framework of C-atoms [14]. Its size, and surface chemistry are precisely controlled during the synthesis. Regarding the surface chemistry, oxo-G possesses hydroxyl, epoxy and organosulfate functional groups. Particularly, the presence of a high number of oxygenated functions makes it attractive for covalent functionalization with different nucleophilic reagents. These characteristics make oxo-G predominantly interesting for applications in different fields, including sensing and energy. For instance, oxo-G has been successfully tested for the preparation of conductive reduced graphene for applications in solar cells [16]. In the biomedical field, the use of oxo-G has been reported to show its ability to overcome cell barriers and sense ribonucleic acids directly in live cells [17].

In this work, we describe the preparation, characterization, and application of oxo-G in gene delivery. For this purpose, two different oxo-G materials have been used, one containing a high percentage of organosulfates (oxo-G1) and one with much lower percentage of the same groups (oxo-G2). Both materials have been modified with low molecular weight polyethyleneimine (PEI) chains. After PEI grafting, the functionalized materials show high binding efficiency for siRNA. Supramolecular investigation and atomistic calculations demonstrate that both functionalized nanomaterials do not induce any evident denaturation of siRNA during the binding process and reveal details of the complexation event at the molecular scale. *In vitro* tests prove that functionalized oxo-G displays high transfection efficacy, inducing gene silencing at extremely low concentration in comparison to oxo-G precursors, unable to complex siRNA. These results evidence the therapeutic potential of oxo-G, foreseeing its application in the gene silencing field.

2. Experimental section

2.1. Synthesis of oxo-G1

One g of oxo-functionalized graphene (oxo-G) containing sulfate groups was synthesized following the earlier reported method that was scaled-up for purposes of this project [18]. Five g of graphite were dispersed in 125 mL conc. sulfuric acid and placed in Teflon reactor that was further cooled down to −10 °C and left for continuous stirring. Ten g of potassium permanganate were added stepwise over a period of 16 h using syringe pump. The reaction was left under continuous stirring for a further 8 h. Next, 125 mL of 20% sulfuric acid were added dropwise over 16 h, and the reaction temperature was continuously kept below 10 °C. After an additional 8 h, the sample was diluted with 250 mL of double distilled water added dropwise over 8 h and left under continuous stirring for a further 16 h. The formation process of oxo-G was fulfilled with stopping of the reaction through dropwise addition of 125 mL of 5% hydrogen peroxide for 1 h. At the end of the reaction, the sample was collected and worked up. First, the sample was washed with double distilled water three times using centrifugation at 1500 RCF (Relative Centrifugal Force) for 9 min each. The collected sample

was filled up with double distilled water and delaminated using the ultrasonication method. For that purpose, the sample was placed into tip sonicator and delaminated with pulse-on-pulse-off set up (20 s on, 20 s off, 4 min). Next, the sample was again washed three times with double distilled water performing centrifugation at 1500 RCF for 15 min, whereas the supernatant was collected each time. The final workup step included centrifugation at 9000 RCF for 45 min, and the precipitate was collected and diluted in double distilled water. The reaction yielded in 540 mg of oxo-G1 in aqueous dispersion at a concentration of 3.6 mg/mL and was further stored at 4 °C.

2.2. Synthesis of oxo-G2

To synthesize oxo-G2, the procedure described above was repeated to produce an additional 1 g of the material, where the sulfur-containing groups were partially cleaved.

The precipitate of the sample oxo-G1 was washed three times with 0.1 M solution of sodium hydroxide under vigorous shaking, followed by centrifugation at 3000 RCF over 15 min each. In the last step, the precipitate was diluted in 0.1 M sodium hydroxide and left for 1 h at temperatures below 10 °C. Final purification steps included washing with double distilled water and centrifugation at 3000 RCF for 15 min repeated three times that was accomplished by collecting precipitate and diluting in double distilled water. This process yielded 330 mg of oxo-G2 in aqueous dispersion at a concentration of 2.2 mg/mL. The dispersion was further stored at 4 °C.

2.3. Characterization of oxo-G1 and oxo-G2

The structural composition of the materials was confirmed by elemental analysis (EA), and the integrity of the carbon lattice was determined by Raman spectroscopy measurements [19]. The as-synthesized oxo-G contains functionalities such as hydroxy groups, epoxides, carboxylic acid groups, as well as sulfur-containing groups like sulfates.

2.4. Determination of lattice defects by Raman spectroscopy

To determine the density of lattice defects of oxo-G1 and oxo-G2, respectively, surface functional groups were reductively removed as follows: the samples were examined on a substrate that was prepared following the procedure described below. For the measurement, each sample was transferred onto a Si/300 nm SiO_2 wafer and air-dried. Next, a few drops of trifluoroacetic acid and hydrogen iodide were placed on the wafer and left on a heat plate for 5 min for reduction of oxygen-containing functionalization resulting in reduced oxo-G materials (r-oxo-G1 and r-oxo-G2). The wafer was washed with double distilled water and air-dried. The samples were then analyzed by Raman spectroscopy. Single- and statistical Raman maps spectra were recorded and evaluated for structural integrity analysis and comparison of the samples, as shown in Fig. S1 and Fig. S2. The recorded statistical Raman maps spectra were evaluated and analyzed by acquisition of Lorentz function. The density of defects was determined following the rationale introduced by Lucchese and Cançado [20].

For r-oxo-G1, the intensity ratio of the I_D/I_G peaks resulted 2.8, and Γ_{2D} value corresponded to 92 cm^{-1} (as shown in Fig. S1). In comparison, r-oxo-G2 sample was characterized by an I_D/I_G ratio of 3.1 with $\Gamma_{2D} = 85$ cm^{-1} as shown in Fig. S2. The density of defects in both materials is to roughly 0.8−1% and can thus be related to a density of defects of also 0.8−1% for oxo-G1 and oxo-G2, respectively [21]. Thus, the lattice integrity is not significantly affected by the treatment with the base.

2.5. Functionalization of oxo-G1 and oxo-G2 and interaction with siRNA

For PEI functionalization, 10 mg of oxo-G1 or oxo-G2 were dispersed in endotoxin free Milli-Q® water to a final volume of 9 mL. In order to reduce the flakes agglomeration during the functionalization process, the dispersion has been stirred using a Ultaturrax t10 with low speed (power 2) [9,22]. Subsequently, 1 ml of 1 mg/mL PEI in endotoxin free Milli-Q® water was added dropwise using a Pasteur pipette. After the Ultraturrax was switched off, the reaction was stirred for 2 days via magnetic agitation. Subsequently, the unreacted PEI has been removed via dialysis using endotoxin free milliQ water (3 days).

2.6. Characterizations

Z-potential values were measured using a Malvern Panalytical Zetasizer Advance Series - Lab (Malvern Instruments) at 25 °C. The four materials were dispersed by bath sonication (15 min) in Milli-Q water (pH 7), acetate buffer (0.05 M, pH 3.6) and ammonia buffer (0.05 M, pH 10) at 1 mg/mL. All the tests were performed three times at 25 °C with 120 s equilibration time. Scanning electron microscopy (SEM) analyses were performed on a Hitachi S-800 electron microscope working at 15 kV. The dispersions at 1 mg/mL were deposited by dip-coating (30 min) on a silicon wafer. Images were treated with FIJI software. Thermogravimetric analysis (TGA) was performed on a TGA1 (Mettler Toledo) apparatus from 30 °C to 900 °C with a ramp of 10 °C/min under N_2 using a flow rate of 50 mL/min^{-1} and platinum pans. X-ray Photoelectron Spectroscopy (XPS) analyses were performed on a Thermo Scientific K-Alpha X-ray photoelectron spectrometer with a basic chamber pressure of 10^{-8}–10^{-9} bar with an anode using Al Kα radiation (hν = 1486.6 eV). The C (1s) photoelectron binding energy was set at 284.5 ± 0.2 eV and used as a reference for calibrating the other peak positions. The samples were analyzed as powder. A spot size of 400 μm was used. The survey spectra are the average of 10 scans with a pass energy of 200.00 eV and a step size of 1 eV. The high-resolution spectra are an average of 10 scans with a pass energy of 50 eV and a step size of 0.1 eV. An ion gun was turned on during analysis. For each sample, the analysis was repeated three times. A solution of double-stranded siRNA (19 bases, Eurogentec control sequence C = 0.1 μg/$μL^{-1}$) was kept constant at 2 μL in every mass ratio. The suspensions of the materials dispersed in Milli-Q® RNAse-free water were prepared corresponding to each mass ratio required for the complexation with siRNA. The suspensions were kept at room temperature for 30 min to allow the formation of the complexes. After staining with Orange DNA loading dye (6 ×, Thermo Fisher Scientific) (total loading sample volume = 30 μL), the suspensions were added to 2% agarose containing GelRed (Biotium, USA) followed by electrophoresis in Tris-Acetate-EDTA (TAE) buffer at 120 mV for 20 min. The gels were then visualized under UV light using the Gel Doc™ EZ Imager – Bio-Rad and Image lab software. The signal of each experiment was normalized to the signal of the free siRNA as a control and subtracted by the background signal by using the ImageJ program. Each experiment was repeated at least three times. Circular dichroism spectra were recorded with a J-810 Jasco spectropolarimeter. Each spectrum was recorded at 1 nm resolution after 32 accumulations from 190 to 350 nm. For this set of experiments 0.08 mg/mL of oxo-G nanomaterials were incubated with 0.04 mg/mL siRNA in Milli-Q® RNAse-free water for 30 min. The spectra were obtained by subtraction of the appropriate blanc. Each spectrum has been recorded three times.

2.7. Molecular dynamics calculations

The adsorption of siRNA on oxo-G surfaces was studied following a methodology based on our previous work [23]. The initial siRNA structure (sequence: UGC-GCU-ACG-AUC-GACGAU-G) was obtained using the nucleic acid builder (NAB) included in AMBER18 [24], with RNA.OL3 forcefield [25,26]. PEI starting structure was built using Discovery Studio Visualizer [27], with protonation state assigned based on recent NMR studies [28] for neutral pH and assigned uniformly. An oxo-G sheet 15 nm × 15 nm large was first created accounting for the two-phase nature of oxidized and unoxidized graphene domains, proper C/O ratio and with no surface defects [29]. Then, sulphate groups and PEI chains were added on both sides of the basal plane. Partial charges were obtained from Kim et al. [30,31]. or derived by the AM1-BCC [32] method where missing; atom types were based on the general amber forcefield [33,34]. All resulting structures were solvated in TIP3P [35] water and counterions (Na^+, Cl^-) added to reach neutralization and make the overall concentration 0.15 M. The boxes were energy minimized, followed by a heating phase to increase the temperature to 300 K under NVT conditions; next, the structures were relaxed under NPT conditions for 100 ns. Time step was 2 fs, periodic boundary conditions, Langevin thermostat and Berendsen barostat were applied, and electrostatic interactions were treated with the particle mesh Ewald [36] procedure. After equilibration, a siRNA and oxo-G structure was extracted, and the oligonucleotide was then placed onto the center of the oxo-G surface at a distance of 6 nm. The resulting complexes were solvated, and counterions added to ensure system neutrality and the desired ionic strength (0.15 M). The structures obtained underwent the same computational procedure as the two components alone, with a production phase of 400 ns. Three different initial configurations for each system were considered. In all simulations, the corners of the oxo-G sheet were kept in place by Cartesian restraints applied to selected atoms to emulate the physical constraint of a larger oxo-G sheet. All simulations were performed with CUDA implementation [37] of AMBER18. Analysis was carried out using CPPTRAJ and NAB module in AMBER18 package, and in-house developed python scripts.

2.8. siRNA silencing

Lipofectamine® RNAiMAX Transfection Reagent (Cat# 13778030), both scrambled (Cat# 4404020) and target Stat3 siRNA (Cat# AM16830), UltraPure DNase/RNase-free distilled water (Cat# 10977035), Tris-acetate-EDTA buffer (TAE; Cat# B49) were purchased from Invitrogen, Thermo Fisher Scientific. Dulbecco's phosphate-buffered saline (DPBS; Cat# 14190250), Dulbecco's Modified Eagle Medium (DMEM; Cat# 31966047), Fetal Bovine Serum (FBS; Cat# 10082147) were obtained from Gibco, Thermo Fisher Scientific. Agarose was purchased from Sigma-Aldrich. iScript cDNA synthesis kit (Cat# 1708891) and SsoAdvanced Universal SYBR Green Supermix (Cat# 1725271) were from Bio-Rad, CA, USA. All primers were obtained and synthesized from Eurogentec, Liège, Belgium. oxo-G/siRNA material complexation: Optimized mass ratio of siRNA and oxo-G material was performed with oxo-G/siRNA corresponding to oxo-G1-PEI/siRNA 1:2, 1:1, 2:1, 3:1 and oxo-G2-PEI/siRNA 1:1, 2:1, 3:1, 4:1). The relative weight of graphene was added to 20 μL of UltraPure water followed by sonicated in a water bath for 10 s. The relative ratio of siRNA was added immediately after the sonication and mix by a vortex. oxo-G/siRNA mixture was then incubated at room temperature for 30 min. The optimized complexed oxo-G/siRNA mixture was determined by loading on 2% agarose gel in 1 × TAE. siRNA transfection: 0.5×10^5

of U-87 MG cells were seeded on 12 wells plate in DMEM supplemented with 10% FBS a day before transfection. Lipofectamine RNAiMAX transfection reagent was used as a positive control for transfection manipulation. Cell transfection was performed as the manufacturer's protocol. For oxo-G material, an optimized ratio of oxo-G/siRNA was used to prepared the complexation with an equal amount of siRNA (approximately 250 ng of siRNA for each well) for cell transfection. The complexation mixture was mixed into serum-free DMEM and added to the cells. Fresh medium (10% FBS, DMEM) was replaced after 12 h of transfection. Total RNA isolation was performed after 48 h of transfection. The experiment was repeated 4 times, each with technical duplicates. For the detection of knockdown Gene expression, total RNA was isolated with Macherey-Nagel NucleoSpin RNA Plus XS kit (Düren, Germany) according to the manufacturer's instruction. The concentration of isolated total mRNA was measured with NanoDrop™ 2000/2000c Spectrophotometers (Thermo Scientific™, MA, USA). The same quantity of RNA template was used for cDNA synthesized by the iScript cDNA synthesis kit following the manufacturer's protocol. qPCR was performed with SsoAdvanced Universal SYBR Green Supermix on the CFX96 Touch Real-Time PCR System (Bio-Rad, CA, USA). The average of RPL6 and RPL27 genes were used as a housekeeping gene to normalize the loading of each sample. Primers were designed using NCBI primer-BLAST web tool, and the primer sequences are shown in Table S3. The $2^{-\Delta\Delta CT}$ method was used to assess the relative mRNA expression. Each sample was analyzed in duplicate. Graph data points were presented by the average expression ratio of each biological replicated to its relative control with a standard error of the mean (S.E.M.).

2.9. Cell viability

The cell proliferation of U-87 MG was measured using MTS assay (Abcam, Cambridge, Cat# ab197010). 1×10^5 cells per mL were seeded at 200 μL per well in a 96-well plate. The day after, 100 μL of medium was removed from each well and replaced by 2× the respective concentration of materials to have a final concentration of 25 μg/mL, 2.5 μg/mL, 0.25 μg/mL and 0.025 μg/mL. The control wells were replaced with fresh medium. At day three, 20 μL of MTS reagent were added to each well, and the cells were incubated for 3 h at 37 °C. The number of viable cells was measured by the absorbance at 490 nm using Berthold technologies TRISTAR LB 941 Microplate reader. The values were normalized using the blanc in respect to each oxo-G concentration. The experiments were repeated 4 times with quadruplicate on each experiment. The data are represented as the of average quadruplicate wells per experiment mean ± SD (Fig. S11). The multiple comparisons for each sample between each concentration and materials were tested by Tukey's multiple comparisons test. The p < 0.05 was considered statistically significant for all analyses.

3. Results and discussion

3.1. Preparation of the materials

Over the last decade, different variants of the Hummers' method have been explored for the production of GO [15]. Oxidative conditions, specifically the addition of permanganate, can also destroy the σ plane leading to the production of CO_2 [14]. This process is associated to the formation of vacancies onto the sheets, with generation of metastable carbon radicals and endoperoxides [15]. Toxicological studies have pointed out the potential harmful response of different non-functionalized GOs to several types of cells and animal models. One of the most plausible mechanisms is the lipidic peroxidation of the membranes induced by the radicals

present on the surface of GO [9]. Recently, a novel protocol for mild oxidation of graphite has been reported by us, leading to the formation of a new type of single layer oxidized form of graphene called oxo-G [14,15]. oxo-G can be produced in similar conditions to GO but keeping the temperature below 10 °C during the oxidation steps. This material shows a controlled chemical structure with low presence of defects (0.01%, about ten times less than GO) and presence of high amounts of oxygenated groups (Figs. S1 and S2). oxo-G was prepared according to the published protocols using $KMnO_4$ as an oxidant for graphite in sulfuric acid [38,39]. During purification, the hydrolysis of organosulfates was prevented by washing with cold water, leading to organosulfate groups covering the surface of oxo-G (sample named oxo-G1). Partial hydrolysis of organosulfates was subsequently achieved by washing with sodium hydroxide solution at 10 °C, followed by extensive washing with water until a pH value of approximately 6 (sample named oxo-G2). oxo-G1 and oxo-G2 display a lateral size of 340 ± 17 nm and 347 ± 19 nm, respectively (Fig. 1).

Exploiting the functional groups and in particular epoxides available onto oxo-G surface, we designed a functional oxo-G suitable for gene silencing [40]. Short molecular weight (800 Da) PEI was selected in order to reduce the known toxicity of high molecular weight PEI [40]. The polymer was grafted onto the flakes through epoxide opening reaction using the "ultra-mixing" method [9]. For this purpose, we used the two types of oxo-G: oxo-G1 with high content of organosulfate (around 3%) and oxo-G2 with low content of organosulfate (around 1%) (Table S1). Following dialysis, prepared dispersions were stored at 4 °C in water. After functionalization, oxo-G1-PEI seems to retain its colloidal stability, while oxo-G2-PEI tends to form little small agglomerates after 24 h. These conjugates were characterized by ζ-potential, thermogravimetric analysis (TGA), derivative thermogravimetric analysis (DTG), and X-Ray photoelectron spectroscopy (XPS).

PEI functionalization induces a strong increase in the ζ-potential of the materials associated to the presence of protonated amines onto oxo-G1-PEI and oxo-G2-PEI (Table S1). oxo-G1 TGA evidenced a two-step mass loss, at 50 and 200 °C, respectively (Fig. 2a black line). This trend is similar to GO behavior, where the first step is associated to the water desorption, while the second, at higher temperature, is due to the loss of oxygenated groups [41]. Functionalization with PEI induces a consistent change of TGA profile (Fig. 2a dotted line). In particular, DTG analysis shows three bands associated with three mass losses at 50, 150, and 330 °C, respectively. While the first mass loss is associated again to water desorption, the decomposition of the organic groups occurred about 50 °C less than in non-functionalized material. This trend can be explained by the functionalization, where epoxide groups are converted and less thermally stable amino groups are present. The mass loss centered at 330 °C (broad peak in the DTG) is associated with the PEI chain decomposition. Similar results were observed in the case of oxo-G2 (Fig. 2c). PEI functionalization also causes a clear change of XPS spectra (Fig. 2b and d). As expected, oxo-G1 and oxo-G2 flakes are highly oxidized graphene sheets mainly composed by C and O, respectively. These results are in strong agreement with the elemental analysis data (Table S2). We did not include sulfur in the XPS atomic percentage since its content is very low and typically requires a long acquisition time. Additionally, using Al Ka X-ray source, the detection limit of S atoms onto the surface has been estimated between 0.3 and 1 atomic %, making in this case elemental analysis much more precise [42]. Functionalization with PEI significantly increases the percentage of nitrogen atoms on the surface of the material up to 8.5% for both oxo-G1 and oxo-G2. When nanomaterial functionalization is performed, it is always appreciable to understand and quantify the reaction conversion grade. Besides, the exact calculation of the functionalization
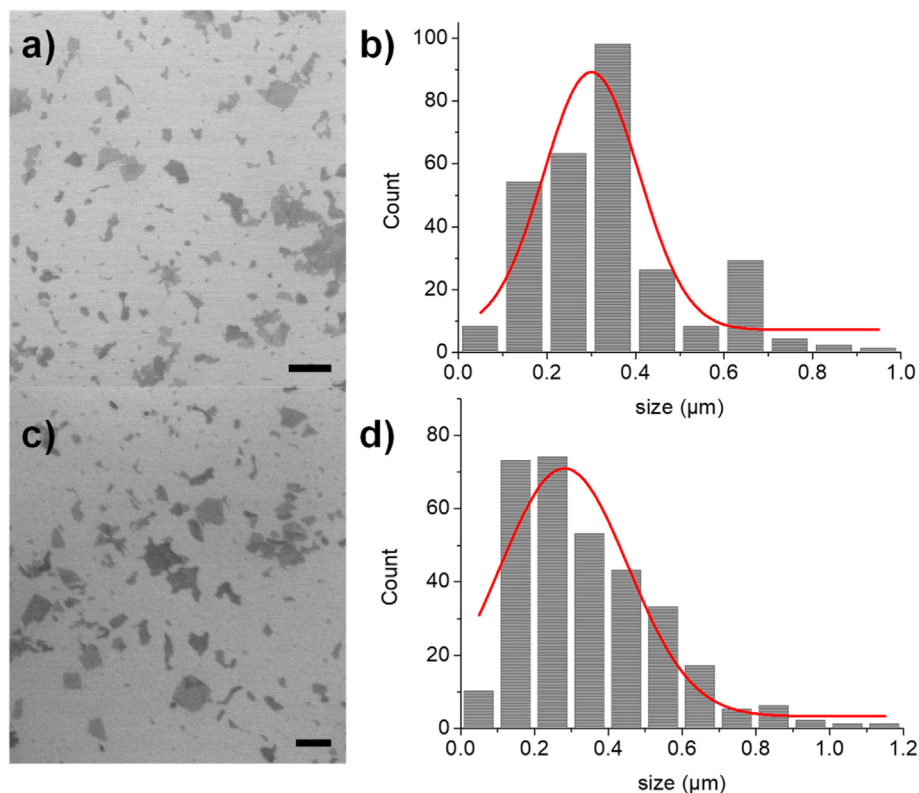
Fig. 1. SEM characterization. a) oxo-G1 SEM image b) lateral distribution of oxo-G1 (n ~300), Gaussian fitting centered at 300 nm. c) oxo-G2 SEM image d) lateral distribution of oxo-G2 (n ~300), Gaussian fitting centered at 281 nm. Scale bar 1 μm. (A colour version of this figure can be viewed online.)

degrees can be tricky due to the complexity of the material surface and to the fact that the most common analytic methods (i.e., HPLC, NMR) cannot be performed. In the case of GO, due to the presence of liable oxygenated groups, TGA is not always reliable, and XPS is preferred [41]. If we consider that PEI has a MW of 800 Da from XPS atomic % (Fig. 2), we can estimate a nitrogen abundance of 6.3 mmol of N per g of conjugate, which roughly corresponds to 1C atom functionalized with PEI out of 100 C atoms for both oxo-G1-PEI and oxo-G2-PEI. This suggests that the presence of sulfate groups is not interfering with the nanomaterials' reactivity with PEI molecules. However, there is a marked difference in the material dispersibility after functionalization, with oxo-G2-PEI forming small agglomerates in solution, while oxo-G1-PEI appears colloidally stable.

3.2. Interaction with siRNA

The capacity of the different oxo-Gs to complex siRNA was investigated through gel retardation assay. For this set of experiments, an appropriate quantity of siRNA (0.2 μg) was incubated for 30 min with the desired quantity of nanomaterial. Subsequently, the dispersions were subjected to gel electrophoresis retardation assay (at 120 V for 20 min). The siRNA complexed to the material cannot migrate, while the free siRNA molecules are able to penetrate into the gel. Gel retardation assays of non-functionalized materials (Fig. S3) showed that both oxo-G1 and oxo-G2 are not able to complex siRNA at a mass ratio up to 50. This is typical for non-functionalized graphene materials. Higher mass ratios were not used because they are less recommended for therapy.

PEI functionalization was able instead to enhance siRNA adsorption by the nanomaterial (Fig. 3). oxo-G1-PEI showed the best complexation capacity adsorbing more than 80% of siRNA

molecules at oxo-G1-PEI/siRNA mass ratio of 2. oxo-G2-PEI displayed less efficiency, where the 80% of the siRNA can be complexed at oxo-G2-PEI/siRNA mass ratio of 5. It is difficult to speculate about the different interactions between oxo-G1-PEI and oxo-G2-PEI with siRNA. Indeed, the functionalization degree of the two materials is similar; hence, the different complexation efficiency cannot be directly attributed to the amino groups present on the surface of the flakes (see also below). Probably, the colloidal stability plays a role in the complexation efficiency, where the more dispersed oxo-G1-PEI is able to adsorb a higher amount of siRNA molecules than the oxo-G2-PEI counterpart does.

We then investigated the nucleic acid complexation from a molecular perspective. Unbiased molecular dynamics (MD) calculations showed that siRNA adsorption might occur on both functionalized and non-functionalized oxo-G surfaces (Figs. 4 and S4). Nonetheless, while this was stable and prolonged for the two oxo-G-PEI and oxo-G2, we observed the detachment of the siRNA during the simulation time for oxo-G1, thus suggesting a weaker interaction for this system. Initially, siRNA fluctuates over all the surfaces. Then, the adsorption is initiated by the anchoring of a terminal bases on the oxo-G surface (Fig. S5) and proceeds with the release of the interfacial water (on average, 1073 water molecules for oxo-G1-PEI, 1069 for oxo-G2-PEI, 41 for oxo-G1, and 38 for oxo-G2), which provides a higher entropic gain to the complexation onto oxo-G-PEI surfaces.

We then analyzed the average number of effective contacts n_c, i.e. the number of any siRNA atoms within a distance of 4 Å from the 2D material, along the binding period (Table 1 and Fig. S6). For both oxo-G-PEI, n_c is almost doubled compared to unfunctionalized systems. This evidences the ability of PEI to promote the formation of supramolecular complexes even when attached on a bidimensional surface. This was not obvious since the grafting of a chain end

5
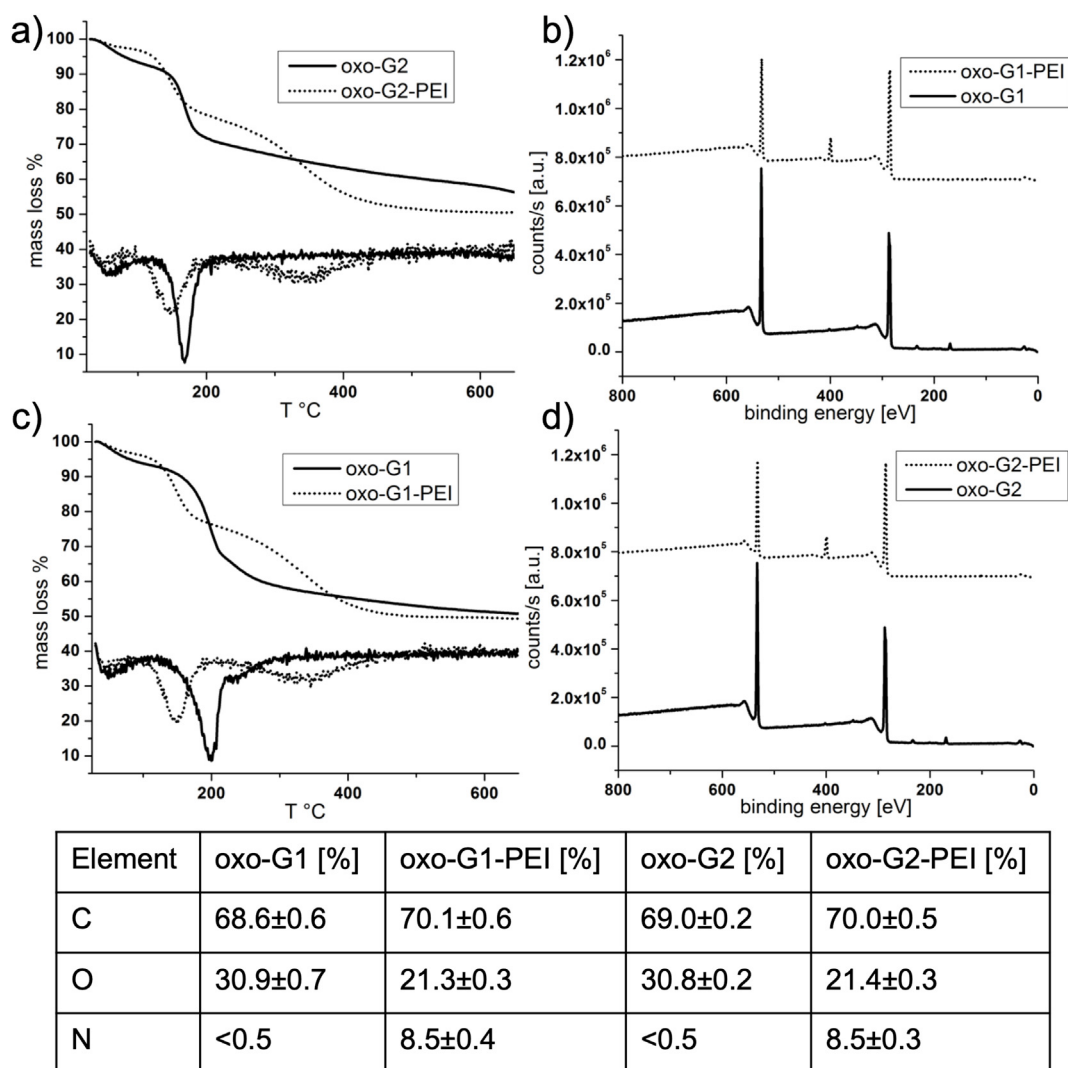
Fig. 2. oxo-G1 (solid line) and oxo-G1-PEI (dotted line) characterizations: a) TGA and DTG; b) XPS survey spectra; oxo-G2 (solid line) and oxo-G2-PEI (dotted line) characterizations c) TGA and DTG; d) XPS survey spectra. Bottom: table reporting the relative XPS atomic percentage of C, O and N.

and the presence of other chains close by might restrict PEI conformational flexibility and alter its well-known ability to establish effective interactions with nucleic acids or other polyelectrolytes.

Calculations of the oxo-G/siRNA interaction energies normalized by the number of contacts allowed to compare and evaluate the interaction efficiency among the systems (Table 1) [43–45]. We see a significantly higher total interaction energy E_{int} for both functionalized oxo-G-PEI surfaces; E_{int} is negative (i.e., still favorable) for oxo-G1 and oxo-G2, but it has very small values, indicating a substantially lower affinity. For oxo-G1, the slightly negative interaction energy is in line with the observed detachment of siRNA during the simulation time. It is worth noting that values associated with oxo-G1-PEI and oxo-G2-PEI are similar. Indeed, the number of contacts established by the biomolecule are comparable in the two systems and almost all of them involve PEI chains. Thus, the oxo-G surface appears relatively screened by PEI, and no major differences in the ability to interact with siRNA are apparent for oxo-G1-PEI and oxo-G2-PEI, at least at the molecular level.

Decomposition of the interaction energy into van der Waals and electrostatic components further reveals that the electrostatic contribution is clearly predominating in oxo-G-PEIs, while for oxo-

G2, the interactions arise from both components, and the electrostatic part is unfavorable for oxo-G1. Hydrogen bond formation (Table 1, n_H) is also contributing to siRNA electrostatic adsorption on oxo-G-PEI. This was confirmed by the calculation of the radial distribution function (RDF) of the PEI nitrogen atoms around electronegative backbone siRNA atoms (Fig. S7). The first peak at ~ 3 Å indeed corresponds to the distance for direct contact between PEI amine groups and siRNA oxygens through hydrogen bonding. The second peak at ~4.4 Å evidences the presence of water-mediating hydrogen bonds, which further stabilizes the binding. The third peak account for weaker indirect interactions, such as hydrogen bonds mediated by two or more water molecules. A much lower hydrogen bonds number n_H is instead detected for oxo-G1 and oxo-G2 (Table 1 and Fig. S8).

Taking all together, atomistic calculations provide evidence that surface functionalization of oxo-G with branched polyamines is a strategy that favors an efficient complexation of siRNA through electrostatic forces and to a lesser extent hydrogen bonds. In addition to binding capacity, preservation of biological activity of the nucleic acid is also crucial for oxo-G-PEI surfaces to be used as a carrier of genes. The integrity depends on the maintenance of the secondary structure, relative arrangements of the sequential
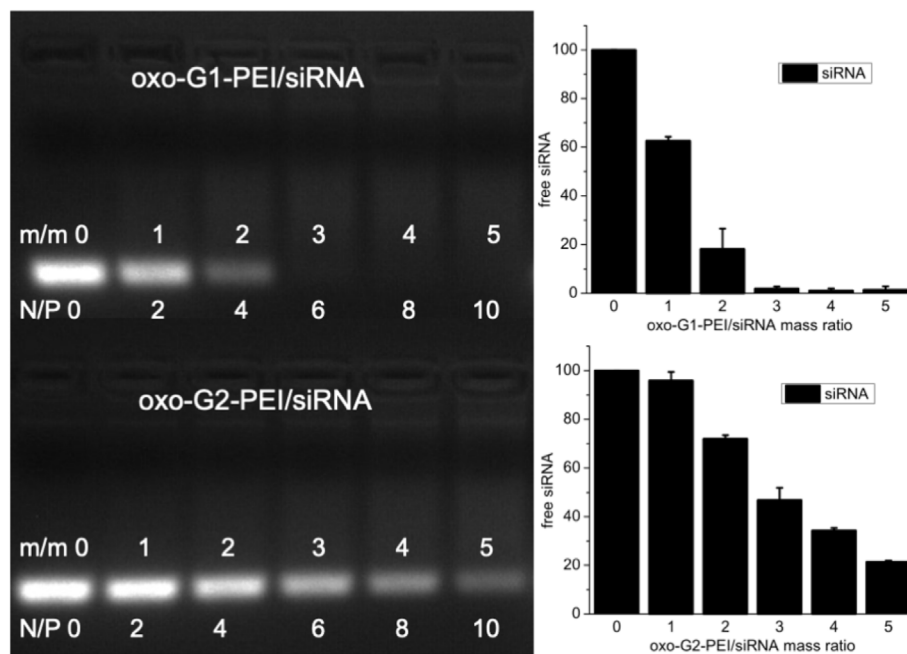
Fig. 3. Gel retardation assay of: top left oxo-G1-PEI and bottom left oxo-G2-PEI with indicated mass (m/m) oxo-G-PEI/siRNA and N/P ratio. Complexation efficiency of: top right oxo-G1-PEI and bottom right oxo-G2-PEI.
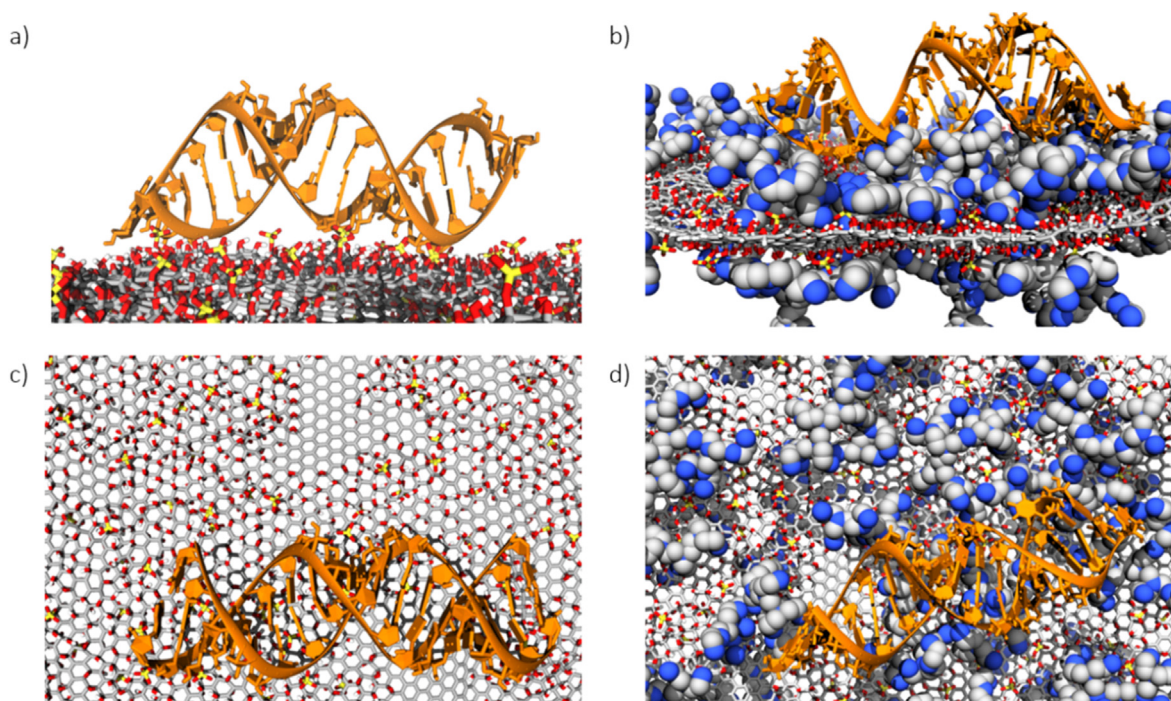
Fig. 4. Snapshots (side and top views) of siRNA on (a−c) oxo-G1 and (b−d) oxo-G1-PEI after physisorption. Color codes for carbon, oxygen, hydrogen, nitrogen and sulfur are grey, red, white, blue, and yellow, respectively. The nucleic acid is depicted in orange. Water molecules and ions are omitted for clarity. (A colour version of this figure can be viewed online.)

nucleobases from the same strand, and hydrogen bond connectivity from complementary strands.

To judge that, we compared the radius of gyration (R_g), Watson-Crick (WC) hydrogen bonds, and interstrand and intrastrand phosphate distance between the sequentially connected nucleobases of the biomolecule in solution and bound. In the absence of 2D material, the nucleic acid is characterized by a R_g of 1.78 ± 0.07 nm and an average of 48 WC hydrogen bonds. After the adsorption, the radius of gyration remains similar, being R_g 1.75 ± 0.06 for oxo-G1-PEI and 1.80 ± 0.05 for oxo-G2-PEI. The number of WC hydrogen bonds is almost preserved (42 for oxo-G1-PEI and 44 for oxo-G2-PEI), with the difference arising mainly from

	n_c [a]	E_{int} [b]	E_{vdw} [b]	E_{ele} [b]	n_H
oxo-G1	531 (35)	−0.16 (0.04)	−0.28 (0.04)	0.12 (0.02)	2 (1)
oxo-G1-PEI	1314 (91)	−25.11 (0.08)	−0.12 (0.01)	−24.99 (0.08)	12 (4)
oxo-G2	763 (74)	−0.77 (0.05)	−0.26 (0.04)	−0.52 (0.03)	5 (2)
oxo-G2-PEI	1252 (125)	−24.87 (0.07)	−0.13 (0.03)	−24.75 (0.06)	10 (3)

[a] A contact is taken into account if any of siRNA atoms is within a cutoff distance of 4 Å with respect to oxo-G.
[b] Normalized by the number of effective contacts. Standard deviations are reported in brackets.

the unpairing of one terminal bases. Comparing the interstrand and intrastrand phosphate distances of the nucleic acid alone and bound to oxo-G-PEI shows that there are no major variations in the duplex conformation (Fig. S9). Thus, the molecular studies suggest that siRNA might preserve the essential structural features after adsorption onto oxo-G-PEI as in its native form.

Previous MD studies have found that the amine groups on linear PEI interact mainly with the oxygen atoms of the phosphate groups of the nucleic acid backbone and while the interactions with electronegative atoms in the nucleic acid groove are less frequent [46]. Here instead, we found that ~ 50% of the effective contacts between PEI charged nitrogen atoms involve O1P and O2P phosphate oxygens, and the remaining contacts are established with other electronegative atoms of the backbone and bases (Table S3). This is likely due to PEI ability of oxo-G-PEI to penetrate deeper within the grooves thanks to its branched nature and specific organization on oxo-G surface [47].

Aiming to better understand the interaction between oxo-G and siRNA, circular dichroism (CD) characterization was performed. For this set of experiments, siRNA was incubated for 30 min with the nanomaterials at mass ratio 2.

Both non-functionalized materials show an intense positive CD signal centered at 225 nm with a shoulder at 300 nm, being the oxo-G1 signal more intense than the signal of oxo-G2 (Fig. 5a and b, black lines). Instead, functionalized oxo-G1-PEI and oxo-G2-PEI show a negligible CD signal (Fig. 5a and b, blue lines). The chiral nature of GO has already been described in the literature [48]. It was asserted that the oxygenated groups, in particular alcohols and epoxides generated during the oxidation process, are associated with the GO chiral behavior. However, the deep understanding of the chiral units responsible for this intense CD signal has not been elucidated yet. Besides, it was seen that reduction of GO and its consequent de-functionalization dramatically reduced the CD signal [48]. In our case, even if oxo-G1 and oxo-G2 show a similar C/O ratio (Fig. 2), the chiral nature of the oxygenated groups may be different, leading to a stronger CD signal in the case of oxo-G1 compared to oxo-G2. An important role can be attributed to the presence of organosulfates on the oxo-G1 surface that may enhance the CD signal with respect to oxo-G2 [14]. We speculate that the surfaces are differently functionalized due to incomplete intercalation of the initial graphite that may lead to different degrees of functionalization of the upper and lower surface, respectively [49]. Further, it is well documented that functional groups on the surface of GO are able to reorganize, a process that depends on storing conditions. Thus, PEI functionalization obviously leads to the rearrangement of functional groups, a behavior, which is also accompanied by racemization.

CD spectrum of siRNA is reported in Fig. 5c and d, showing a typical profile of the A-helix conformation where the positive band (260 nm) is due to the base-base pairing, while the negative signal (210 nm) is associated with the phosphate backbone [50]. When siRNA is incubated with oxo-G1, there is a significant change in the CD spectrum of siRNA with the appearance of a negative band centered at 230 nm with a shoulder at 290 nm. In the case of oxo-G2, the CD spectrum of the oligonucleotide is retained. We have already demonstrated that the interaction of GO with siRNA is a dynamic equilibrium, where the nucleic acid molecules are able to adsorb and desorb from the surface of the sheets [50]. CD evidenced a clear A-helix RNA alteration induced by the oxo-G1 interaction. A similar CD profile was found in the literature, where guanosine nucleobases were assembly during Ag nanoparticles formation [51]. The authors associated this CD signal with the agglomeration of the nucleobases onto the nanoparticle surface [51]. In the case of oxo-G1, the dramatic changes of siRNA secondary structure cannot be attributed to a significant complexation since the nanomaterial has a negligible affinity for the double-strand as evidenced from gel electrophoresis and molecular dynamics calculations (Fig. S3). oxo-G2 instead does not seem to alter the A-helix structure. Considering that the size and physical properties of the two materials are the same, the nature of this difference could lie in the organosulfate groups present onto the oxo-G1 flakes. Lastly, PEI functionalized materials do not seem to alter the A-helix RNA structure (Fig. 5c and d) and so they should not alter its biological activity.

3.3. Biological study

Finally, PEI functionalized oxo-G1 and oxo-G2 were applied for gene silencing in vitro. Pre-designed Stat3 targeted siRNA was used to knockdown Stat3 expression in U-87 MG cells. From the gene retardation results (Fig. 3), we have decided to conduct the in vitro tests at oxo-G-PEI/siRNA of 1:1 and 2:1 ratios for oxo-G1-PEI and oxo-G2-PEI, respectively. A scrambled siRNA was used as a negative control. Total mRNA was isolated 48 h post-transfection and processed for cDNA following RT-qPCR. The targeted relative mRNA expression of each group was significantly downregulated when compared to the scrambled siRNA (Fig. 6). There was no significate difference between the transfection methods, assessed by one-way ANOVA with Tukey's test. Data suggested that both oxo-G1-PEI and oxo-G2-PEI can be used as a siRNA transfection carrier.

In order to exclude that the different graphene conjugates affect the viability of the cells, U-87 MG cell proliferation was tested with MTS assay. The result showed no significant difference on cell proliferation compared to the control group, except oxo-G1-PEI at the highest concentration (25 μg/mL). Although this value has a significant difference with *p-value* at 0.0381, it is 100 times more concentrated than the working concentration of the silencing experiment, and the cell viability remains higher than 50% (Fig. 7).

The difference in the optimized mass ratio for silencing (Fig. 6) indicated that two times more oxo-G2-PEI is needed to transfect the same number of cells compared to oxo-G1-PEI. In this case, 500 ng of oxo-G2-PEI was employed to transfect 0.5×10^5 U-87 MG cells, whereas only 250 ng of oxo-G1-PEI was used. Lee et al. have reported the use of GO nano-wrap for silencing with a dose of 170 pg of material per cell [52]. Similar results have been reported by Liu et al. where 500 ng per cell of GO functionalized with cisplatin were used for delivery of siRNA in vitro [53]. More recently, Ou et al. have reported GO functionalized with PEI exhibiting good silencing efficacy at 100 pg of material per cell. In our case, we obtain a significant silencing effect at a dose of 5 and 10 pg/cell for oxo-G1-PEI and oxo-G2-PEI, respectively. These concentrations are up to three orders of magnitude lower than those reported in the literature using GO for gene silencing. It is difficult to understand why oxo-G-PEI shows such an efficient silencing efficacy. Compared to the previous works [6], oxo-G1 and oxo-G2 display a higher dispersibility. Additionally, the "ultramixig" method allows a high
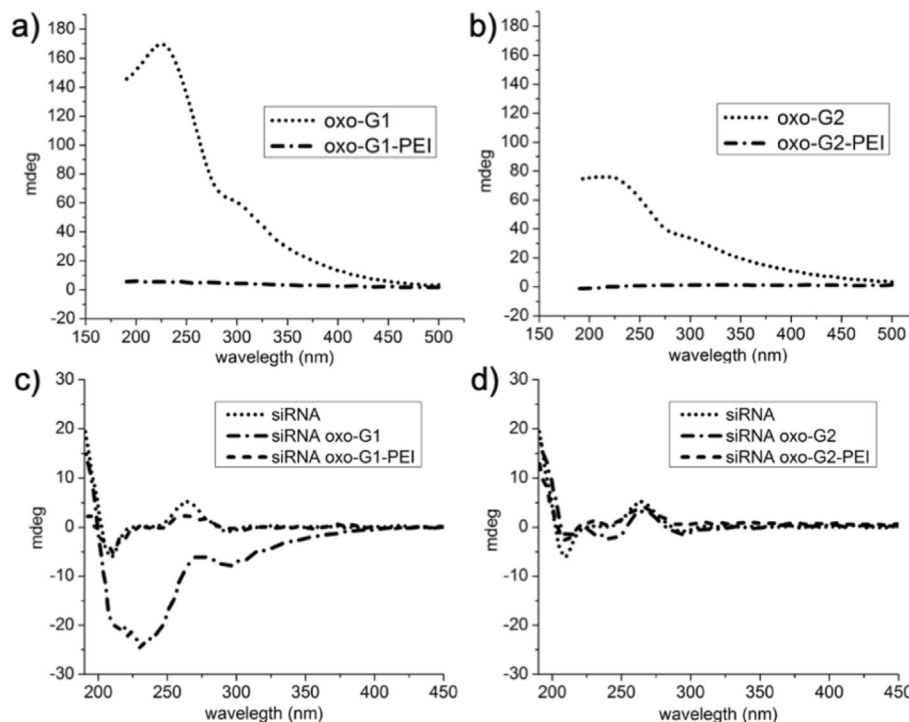
Fig. 5. Circular dichroism characterization of a) oxo-G1 and oxo-G1-PEI, b) oxo-G2 and oxo-G2-PEI, siRNA incubated c) with oxo-G1 and oxo-G1-PEI d) oxo-G2 and oxo-G2-PEI.

functionalization degree (Fig. 2) without compromising the colloidal stability of the materials (Table S1). These facts may enhance the surface area available for siRNA adsorption and

delivery. The high protection imparted by oxo-G1-PEI and oxo-G2-PEI to the siRNA molecules in solution (Fig. 5) and *in vitro* (RNA quantified 48 h after administration), together with the high performances in RNA downregulation, demonstrate that oxo-G is a powerful tool for gene silencing.
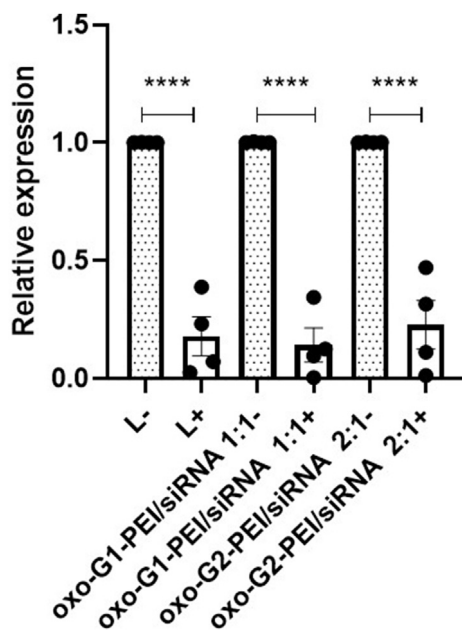
Fig. 6. Detection of Stat3 knockdown by RT-qPCR. U-87 MG were treated with Stat3 targeted siRNA (+) and scrambler siRNA (−) with Lipofectamine RNAiMAX transfection reagent and oxo-G1-PEI and oxo-G2-PEI. The Stat3 gene mRNA transcript level at 48 h post-transfection was analyzed by RT-qPCR. The relative mRNA expression level was used scrambler siRNA sample as control (n = 4, S.E.M.). oxo-G1-PEI and oxo-G2-PEI were tested at 1:1 and 2:1 oxo-G/siRNA mass ratios, respectively. Data showed ****p < 0.0001 indicate statistically significant difference, assessed by one-way ANOVA.

4. Conclusions

In this work, we have reported the application of functionalized oxo-G for gene silencing. Two different oxo-G materials were used, with different contents in organosulfate groups. Aiming to enhance the affinity of oxo-G1 and oxo-G2 for siRNA, the two nanomaterials were functionalized with PEI. Gel retardation assays show that PEI functionalized materials are able to stably adsorb siRNA molecules at low mass ratio. Moreover, supramolecular studies by CD and MD calculations demonstrate that the functionalized materials do not cause any evident alteration of RNA native helical conformation and disclose the foundations of the interaction between oxo-G-PEI and siRNA. Finally, *in vitro* tests show that both oxo-G1-PEI and oxo-G2-PEI are able to efficiently deliver siRNA and induce efficiently gene silencing at a concentration up to 20 times lower than the one reported in the literature (5 pg/cell against 100 pg/cell reported in the literature) [6]. Additionally, similar strategies have been reported for *in vivo* silencing of osteosarcoma and for liver cancer treatment [6,7]. The present oxo-G-PEI structures can be used for *in vivo* gene silencing through intratumoral injection. Moreover, oxo-G platforms allow multi-functionalization (e.g., anchoring other drugs or targeting agents) and are photothermal agents making them interesting for combined targeted gene delivery and drug delivery or phototherapy. These results show the good applicability of oxo-G in gene silencing, foreseeing its further drug and gene delivery applications.
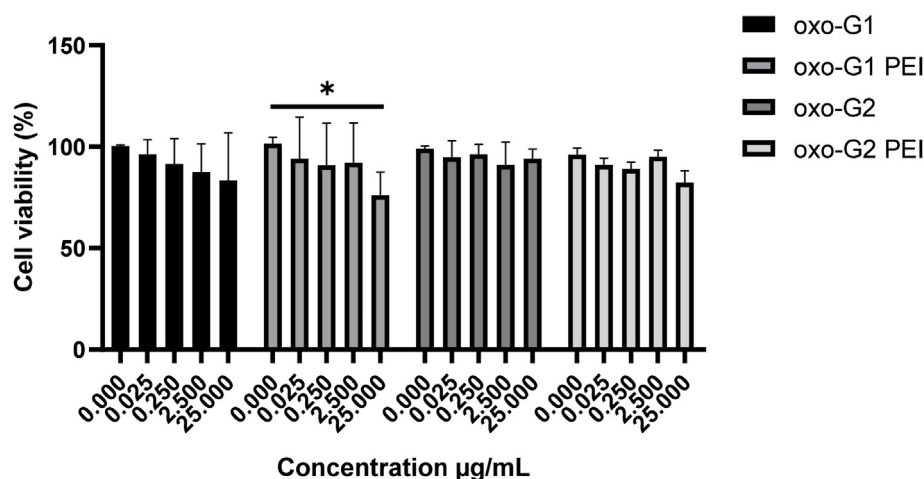
Fig. 7. Cell proliferation was assessed via MTS assay at the with different concentration of oxo-G1, oxo-G2, oxo-G1-PEI and oxo-G2-PEI. Results represent the mean ± SD (n = 4). There is a significant different which p = 0.0381 between control and 25 μg/mL of Oxo-G1-PEI, which is 100 times more concentrated than the concentration used for the gene silencing experiment.

CRediT authorship contribution statement

Giacomo Reina, Cristian Gabellini, Maria Maranska, Fabian Grote, Shan Min Chin, Lucas Jacquemin: Performed experiments, analyzed the results, **Giacomo Reina, Shan Min Chin**: Wrote the manuscript, **François Berger, Paola Posocco, Siegfried Eigler, Alberto Bianco**: Supervised the project, provided funding, discussed the results, reviewed and wrote the manuscript.

Declaration of competing interest

The authors declare that they have no known competing financial interests or personal relationships that could have appeared to influence the work reported in this paper.

References

[1] K. Kaygisiz, C.V. Synatschke, Materials promoting viral gene delivery, Biomater. Sci. 8 (2020) 6113–6156, https://doi.org/10.1039/D0BM01367F.

[2] S. Bouziana, D. Bouzianas, Anti-CD19 CAR-T cells: digging in the dark side of the golden therapy, Crit. Rev. Oncol. Hematol. 157 (2021) 103096, https://doi.org/10.1016/J.CRITREVONC.2020.103096.

[3] L.A. Jackson, E.J. Anderson, N.G. Rouphael, P.C. Roberts, M. Makhene, R.N. Coler, M.P. McCullough, J.D. Chappell, M.R. Denison, L.J. Stevens, A.J. Pruijssers, A. McDermott, B. Flach, N.A. Doria-Rose, K.S. Corbett, K.M. Morabito, S. O'Dell, S.D. Schmidt, P.A. Swanson, M. Padilla, J.R. Mascola, K.M. Neuzil, H. Bennett, W. Sun, E. Peters, M. Makowski, J. Albert, K. Cross, W. Buchanan, R. Pikaart-Tautges, J.E. Ledgerwood, B.S. Graham, J.H. Beigel, An mRNA vaccine against SARS-CoV-2 — preliminary report, N. Engl. J. Med. 383 (2020) 1920–1931, https://doi.org/10.1056/nejmoa2022483/suppl_file/nejmoa2022483_data-sharing.pdf.

[4] X. Gao, L. Li, X. Cai, Q. Huang, J. Xiao, Y. Cheng, Targeting nanoparticles for diagnosis and therapy of bone tumors: opportunities and challenges, Biomaterials 265 (2021) 120404, https://doi.org/10.1016/j.biomaterials.2020.120404.

[5] Y. Yin, T.L. Nguyen, B. Wang, H.T.T. Duong, D.S. Lee, J.H. Kim, J. Kim, J.H. Jeong, Simultaneous delivery of DNA vaccine and hydrophobic adjuvant using reducible polyethylenimine-functionalized graphene oxide for activation of dendritic cells, J. Ind. Eng. Chem. 80 (2019) 870–876, https://doi.org/10.1016/j.jiec.2019.08.038.

[6] L. Ou, H. Lin, Y. Song, G. Tan, X. Gui, J. Li, X. Chen, Z. Deng, S. Lin, Efficient miRNA inhibitor with GO-PEI nanosheets for osteosarcoma suppression by targeting PTEN, Int. J. Nanomed. 15 (2020) 5131, https://doi.org/10.2147/ijn.s257084.

[7] Y. Qu, F. Sun, F. He, C. Yu, J. Lv, Q. Zhang, D. Liang, C. Yu, J. Wang, X. Zhang, A. Xu, J. Wu, Glycyrrhetinic acid-modified graphene oxide mediated siRNA delivery for enhanced liver-cancer targeting therapy, Eur. J. Pharmaceut. Sci. 139 (2019) 105036, https://doi.org/10.1016/j.ejps.2019.105036.

[8] N.Y. Kim, S. Blake, D. De, J. Ouyang, J. Shi, N. Kong, Two-dimensional nanosheet-based photonic nanomedicine for combined gene and photothermal therapy, Front. Pharmacol. 10 (2020) 1573, https://doi.org/10.3389/fphar.2019.01573/bibtex.

[9] G. Reina, A. Ruiz, D. Murera, Y. Nishina, A. Bianco, Ultramixing, A simple and effective method to obtain controlled and stable dispersions of graphene oxide in cell culture media, ACS Appl. Mater. Interfaces 11 (2019) 7695–7702, https://doi.org/10.1021/acsami.8b18304.

[10] C.C. Liu, J.J. Zhao, R. Zhang, H. Li, B. Chen, L.L. Zhang, H. Yang, Multifunctionalization of graphene and graphene oxide for controlled release and targeted delivery of anticancer drugs, Am. J. Transl. Res. 9 (2017) 5197.

[11] D. Plachá, J. Jampilek, Graphenic materials for biomedical applications, Nanomaterials (2019) 1758, https://doi.org/10.3390/nano9121758. Vol. 9, Page 1758. 9 (2019).

[12] C. Martín, K. Kostarelos, M. Prato, A. Bianco, Biocompatibility and biodegradability of 2D materials: graphene and beyond, Chem. Commun. 55 (2019) 5540–5546, https://doi.org/10.1039/c9cc01205b.

[13] B. Fadeel, C. Bussy, S. Merino, E. Vázquez, E. Flahaut, F. Mouchet, L. Evariste, L. Gauthier, A.J. Koivisto, U. Vogel, C. Martín, L.G. Delogu, T. Buerki-Thurnherr, P. Wick, D. Beloin-Saint-Pierre, R. Hischier, M. Pelin, F. Candotto Carniel, M. Tretiach, F. Cesca, F. Benfenati, D. Scaini, L. Ballerini, K. Kostarelos, M. Prato, A. Bianco, Safety assessment of graphene-based materials: focus on human health and the environment, ACS Nano 12 (2018) 10582–10620, https://doi.org/10.1021/acsnano.8b04758.

[14] S. Eigler, Controlled chemistry approach to the oxo-functionalization of graphene, Chem. Eur J. 22 (2016) 7012–7027, https://doi.org/10.1002/CHEM.201600174.

[15] S. Eigler, A. Hirsch, Controlled functionalization of graphene by oxo-addends, Phys. Sci. Rev. (2017) 230–266, https://doi.org/10.1515/9783110284645-003/html.

[16] M. Li, W.-W. Zuo, Q. Wang, K.-L. Wang, M.-P. Zhuo, H. Köbler, C.E. Halbig, S. Eigler, Y.-G. Yang, X.-Y. Gao, Z.-K. Wang, Y. Li, A. Abate, M. Li, K. Wang, M. Zhuo, Z. Wang, W. Zuo, Q. Wang, H. Köbler, A. Abate, Y.F. Li, C.E. Halbig, S. Eigler, Y. Yang, X. Gao, Ultrathin nanosheets of oxo-functionalized graphene

inhibit the ion migration in perovskite solar cells, Adv. Energy Mater. 10 (2020) 1902653, https://doi.org/10.1002/aenm.201902653.

[17] H. Pieper, C.E. Halbig, L. Kovbasyuk, M.R. Filipovic, S. Eigler, A. Mokhir, Oxo-functionalized graphene as a cell membrane carrier of nucleic acid probes controlled by aging, Chem. Eur J. 22 (2016) 15389–15395, https://doi.org/10.1002/chem.201603063.

[18] S. Eigler, M. Enzelberger-Heim, S. Grimm, P. Hofmann, W. Kroener, A. Geworski, C. Dotzer, M. Röckert, J. Xiao, C. Papp, O. Lytken, H.P. Steinrück, P. Müller, A. Hirsch, Wet chemical synthesis of graphene, Adv. Mater. 25 (2013) 3583–3587, https://doi.org/10.1002/adma.201300155.

[19] A.C. Ferrari, D.M. Basko, Raman spectroscopy as a versatile tool for studying the properties of graphene, Nat. Nanotechnol. (2013) 235–246, https://doi.org/10.1038/nnano.2013.46, 84. 8 (2013).

[20] Y.Y. Wang, Z.H. Ni, T. Yu, Z.X. Shen, H.M. Wang, Y.H. Wu, W. Chen, A.T.S. Wee, Raman studies of monolayer graphene: the substrate effect, J. Phys. Chem. C 112 (2008) 10637–10640, https://doi.org/10.1021/jp8008404.

[21] S. Eigler, C. Dotzer, A. Hirsch, Visualization of defect densities in reduced graphene oxide, Carbon 50 (2012) 3666–3673, https://doi.org/10.1016/J.CARBON.2012.03.039.

[22] C. Martín, A. Ruiz, S. Keshavan, G. Reina, D. Murera, Y. Nishina, B. Fadeel, A. Bianco, A biodegradable multifunctional graphene oxide platform for targeted cancer therapy, Adv. Funct. Mater. 29 (2019), https://doi.org/10.1002/adfm.201901761.

[23] I. De Lázaro, S. Vranic, D. Marson, A.F. Rodrigues, M. Buggio, A. Esteban-Arranz, M. Mazza, P. Posocco, K. Kostarelos, Graphene oxide as a 2D platform for complexation and intracellular delivery of siRNA, Nanoscale 11 (2019) 13863–13877, https://doi.org/10.1039/c9nr02301a.

[24] A.T. Bogetti, H.E. Piston, J.M.G. Leung, C.C. Cabalteja, D.T. Yang, A.J. Degrave, K.T. Debiec, D.S. Cerutti, D.A. Case, W.S. Horne, L.T. Chong, A twist in the road less traveled: the AMBER ff15ipq-m force field for protein mimetics, J. Chem. Phys. 153 (2020), https://doi.org/10.1063/5.0019054.

[25] A. Pérez, I. Marchán, D. Svozil, J. Sponer, T.E. Cheatham, C.A. Laughton, M. Orozco, Refinement of the AMBER force field for nucleic acids: improving the description of α/γ conformers, Biophys. J. 92 (2007) 3817–3829, https://doi.org/10.1529/biophysj.106.097782.

[26] M. Zgarbová, M. Otyepka, J. Šponer, A. Mládek, P. Banáš, T.E. Cheatham, P. Jurečka, Refinement of the Cornell et al. Nucleic acids force field based on reference quantum chemical calculations of glycosidic torsion profiles, J. Chem. Theor. Comput. 7 (2011) 2886–2902, https://doi.org/10.1021/ct200162a/suppl_file/ct200162x_si_001.pdf.

[27] S.A. Mir, A. Firoz, M. Alaidarous, B. Alshehri, A.A. Bin Dukhyil, S. Banawas, S.A. Alsagaby, W. Alturaiki, G.A. Bhat, F. Kashoo, A.M. Abdel-Hadi, Identification of SARS-CoV-2 RNA-dependent RNA polymerase inhibitors from the major phytochemicals of Nigella sativa: an in silico approach, Saudi J. Biol. Sci. 29 (2022) 394–401, https://doi.org/10.1016/j.sjbs.2021.09.002.

[28] D.R. Holycross, M. Chai, Comprehensive NMR studies of the structures and properties of PEI polymers, Macromolecules 46 (2013) 6891–6897, https://doi.org/10.1021/MA4011796.

[29] B. Butz, C. Dolle, C.E. Halbig, E. Rdmann Spiecker, S. Eigler, [B Butz,] C Dolle, E. Spiecker, C.E. Halbig, S. Eigler, Highly intact and pure oxo-functionalized graphene: synthesis and electron-beam-induced reduction, Angew. Chem. Int. Ed. 55 (2016) 15771–15774, https://doi.org/10.1002/anie.201608377.

[30] H.S. Kim, B.L. Farmer, Y.G. Yingling, Physisorption: effect of graphene oxidation rate on adsorption of poly-thymine single stranded DNA, Adv. mater. interfaces 4 (2017), https://doi.org/10.1002/admi.201770036. Adv. Mater. Interfaces 8/2017.

[31] D. Stauffer, N. Dragneva, W.B. Floriano, R.C. Mawhinney, G. Fanchini, S. French, O. Rubel, An atomic charge model for graphene oxide for exploring its bioadhesive properties in explicit water, J. Chem. Phys. 141 (2014), 044705, https://doi.org/10.1063/1.4890503.

[32] A. Jakalian, B.L. Bush, D.B. Jack, C.I. Bayly, Fast, efficient generation of high-quality atomic charges. AM1-BCC model: I. Method, J. Comput. Chem. 21 (2000) 132–146, https://doi.org/10.1002/(sici)1096-987x(20000130)21:2.

[33] J. Wang, W. Wang, P.A. Kollman, D.A. Case, Automatic atom type and bond type perception in molecular mechanical calculations, J. Mol. Graph. Model. 25 (2006) 247–260, https://doi.org/10.1016/J.JMGM.2005.12.005.

[34] J. Wang, R.M. Wolf, J.W. Caldwell, P.A. Kollman, D.A. Case, Development and testing of a general amber force field, J. Comput. Chem. 25 (2004) 1157–1174, https://doi.org/10.1002/jcc.20035.

[35] W.L. Jorgensen, J. Chandrasekhar, J.D. Madura, R.W. Impey, M.L. Klein, Comparison of simple potential functions for simulating liquid water, J. Chem. Phys. 79 (1998) 926, https://doi.org/10.1063/1.445869.

[36] T. Darden, D. York, L. Pedersen, Particle mesh Ewald: an N•log(N) method for Ewald sums in large systems, J. Chem. Phys. 98 (1998) 10089, https://doi.org/10.1063/1.464397.

[37] R. Salomon-Ferrer, A.W. Götz, D. Poole, S. Le Grand, R.C. Walker, Routine microsecond molecular dynamics simulations with AMBER on GPUs. 2. Explicit solvent particle mesh ewald, J. Chem. Theor. Comput. 9 (2013) 3878–3888, https://doi.org/10.1021/ct400314y/suppl_file/ct400314y_si_001.pdf.

[38] S. Eigler, C. Dotzer, F. Hof, W. Bauer, A. Hirsch, Sulfur species in graphene oxide, Chem. Eur J. 19 (2013) 9490–9496, https://doi.org/10.1002/CHEM.201300387.

[39] P. Feicht, J. Biskupek, T.E. Gorelik, J. Renner, C.E. Halbig, M. Maranska, F. Puchtler, U. Kaiser, S. Eigler, Brodie's or Hummers' method: oxidation conditions determine the structure of graphene oxide, Chem. Eur J. 25 (2019) 8955–8959, https://doi.org/10.1002/chem.201901499.

[40] N.D.Q. Chau, G. Reina, J. Raya, I.A. Vacchi, C. Ménard-Moyon, Y. Nishina, A. Bianco, Elucidation of siRNA complexation efficiency by graphene oxide and reduced graphene oxide, Carbon 122 (2017) 643–652, https://doi.org/10.1016/j.carbon.2017.07.016.

[41] I.A. Vacchi, C. Spinato, J. Raya, A. Bianco, C. Ménard-Moyon, Chemical reactivity of graphene oxide towards amines elucidated by solid-state NMR, Nanoscale 8 (2016) 13714–13721, https://doi.org/10.1039/c6nr03846h.

[42] A.G. Shard, Detection limits in XPS for more than 6000 binary systems using Al and Mg Kα X-rays, Surf. Interface Anal. 46 (2014) 175–185, https://doi.org/10.1002/SIA.5406.

[43] C. Chen, P. Posocco, X. Liu, Q. Cheng, E. Laurini, J. Zhou, C. Liu, Y. Wang, J. Tang, V.D. Col, T. Yu, S. Giorgio, M. Fermeglia, F. Qu, Z. Liang, J.J. Rossi, M. Liu, P. Rocchi, S. Pricl, L. Peng, Mastering dendrimer self-assembly for efficient siRNA delivery: from conceptual design to in vivo efficient gene silencing, Small 12 (2016) 3667–3676, https://doi.org/10.1002/smll.201503866.

[44] A. Barnard, P. Posocco, M. Fermeglia, A. Tschiche, M. Calderon, S. Pricl, D.K. Smith, Double-degradable responsive self-assembled multivalent arrays – temporary nanoscale recognition between dendrons and DNA, Org. Biomol. Chem. 12 (2013) 446–455, https://doi.org/10.1039/c3ob42202j.

[45] T.K. Mukhopadhyay, A. Datta, Screening two dimensional materials for the transportation and delivery of diverse genetic materials, Nanoscale 12 (2020) 703–719, https://doi.org/10.1039/c9nr05930j.

[46] J.D. Ziebarth, D.R. Kennetz, N.J. Walker, Y. Wang, Structural comparisons of PEI/DNA and PEI/siRNA complexes revealed with molecular dynamics simulations, J. Phys. Chem. B 121 (2017) 1941–1952, https://doi.org/10.1021/acs.jpcb.6b10775/suppl_file/jp6b10775_si_001.pdf.

[47] H.S. Antila, M. Härkönen, M. Sammalkorpi, Chemistry specificity of DNA–polycation complex salt response: a simulation study of DNA, polylysine and polyethyleneimine, Phys. Chem. Chem. Phys. 17 (2015) 5279–5289, https://doi.org/10.1039/c4cp04967e.

[48] J. Cao, H.J. Yin, R. Song, Circular dichroism of graphene oxide: the chiral structure model, Front. Mater. Sci. 7 (2013) 83–90, https://doi.org/10.1007/s11706-013-0192-x, 2013 71.

[49] S. Seiler, C.E. Halbig, F. Grote, P. Rietsch, F. Börrnert, U. Kaiser, B. Meyer, S. Eigler, Effect of friction on oxidative graphite intercalation and high-quality graphene formation, Nat. Commun. 91 (2018) 9, https://doi.org/10.1038/s41467-018-03211-1 (2018) 1–9.

[50] G. Reina, N.D.Q. Chau, Y. Nishina, A. Bianco, Graphene oxide size and oxidation degree govern its supramolecular interactions with siRNA, Nanoscale 10 (2018) 5965–5974, https://doi.org/10.1039/c8nr00333e.

[51] O. Pandoli, A. Massi, A. Cavazzini, G.P. Spada, D. Cui, Circular dichroism and UV-Vis absorption spectroscopic monitoring of production of chiral silver nanoparticles templated by guanosine 5′-monophosphate, Analyst 136 (2011) 3713–3719, https://doi.org/10.1039/c1an15288b.

[52] J.E. Lee, K. Lee, J.A. Nam, A. Kim, S.Y. Lee, M.S. Lee, N.W. Kim, Y. Yin, J.W. Park, S.Y. Park, J.H. Jeong, Cellular delivery of siRNA using Poly(2-dimethylaminoethyl methacrylate)- functionalized graphene oxide nanowrap, Macromol. Res. 26 (2018) 1115–1122, https://doi.org/10.1007/s13233-019-7017-4, 2018 2612.

[53] P. Liu, S. Wang, X. Liu, J. Ding, W. Zhou, Platinated graphene oxide: a nanoplatform for efficient gene-chemo combination cancer therapy, Eur. J. Pharmaceut. Sci. 121 (2018) 319–329, https://doi.org/10.1016/j.ejps.2018.06.009.